J. Fluid Mech. (2015), *vol.* 765, *pp.* 396–423.
doi:10.1017/jfm.2014.732

Direct numerical simulation of low-Reynolds-number flow past arrays of rotating spheres

Qiang Zhou[1] **and Liang-Shih Fan**[1,†]

[1]Department of Chemical and Biomolecular Engineering, The Ohio State University, Columbus, OH 43210, USA

(Received 1 May 2014; revised 13 November 2014; accepted 15 December 2014; first published online 22 January 2015)

Immersed boundary-lattice Boltzmann simulations are used to examine the effects of particle rotation, at low particle Reynolds numbers, on flows in ordered and random arrays of mono-disperse spheres. The drag force, the Magnus lift force and the torque on the spheres, are determined at solid volume fractions up to the close-packed limits of the arrays. The rotational Reynolds number based on the angular velocity and the diameter of the spheres is used to characterize the rotational movement of spheres. The results show that the normalized Magnus lift force produced by particle rotation is approximately in direct proportion to the rotational Reynolds number, while the normalized drag force and torque acting on spheres are barely affected by this number. The Magnus lift force is negligible relative to the magnitude of the drag force when the rotational Reynolds number is low. However, it can be very significant, and even larger than the drag force, as the rotational Reynolds number increases up to $O(10^2)$, especially for low solid volume fractions. Based on the simulation results, relations for the Magnus lift force and the torque for both ordered arrays and random arrays of rotating spheres at solid volume fractions from zero to close-packed limits are formulated. Further, the drag force relations in the literature are revised based on existing theories and the present simulation results for both arrays of spheres.

Key words: multiphase and particle-laden flows, particle/fluid flows

1. Introduction

It is known that a spinning object moving in a viscous fluid experiences a force orthogonal to the plane spanned by the direction of the object's translational motion and its spin axis. This force accounts for the curved trajectory of spinning balls in sports such as soccer, tennis and golf. This transverse force, now usually termed the Magnus lift force, was first experimentally observed on spinning spheres by Robins in 1742 and then on rotating cylinders by Magnus in 1853 (Barkla & Auchterlonie 1971). The explanation for this phenomenon was not given until the introduction of boundary-layer theory by Prandtl in 1904 (see Anderson 2005). Considering the object

†Email address for correspondence: fan.1@osu.edu

to be a sphere, the particle Reynolds number (usually referred to as Reynolds number for conciseness) used to characterize the flow dynamics is usually defined as

$$Re = \rho\,|\boldsymbol{U}|\,d/\mu \tag{1.1}$$

where $\boldsymbol{U}$ is the steady-state superficial fluid velocity, defined as the fluid velocity averaged over the total volume of the system, d is the diameter of the sphere, and ρ and μ are the density and the dynamic viscosity of the fluid, respectively. The Reynolds numbers at which the aforementioned phenomena occur are usually very large. This paper will focus on computing the Magnus lift force for small values of the Reynolds number and hence the primary cause of the lift force for large Reynolds numbers, flow separation, is no longer involved in the flow dynamics. In the range of low Reynolds numbers, the Magnus effect is a particular manifestation of Bernoulli's theorem and the lift force is mainly generated by the pressure differences on opposite sides of the spinning object.

Rubinow & Keller (1961) theoretically calculated the lift force caused by particle rotation at low Reynolds numbers. The lift force can be expressed as

$$\boldsymbol{F}_L = -\pi d^3 \rho \boldsymbol{\omega} \times \boldsymbol{U}/8, \tag{1.2}$$

where $\boldsymbol{\omega}$ is the angular velocity of the sphere. Dividing the lift force by the Stokes drag

$$\boldsymbol{F}_{DS} = 3\pi d\mu \boldsymbol{U}, \tag{1.3}$$

we have the magnitude of the normalized lift force as follows:

$$F_L = Re_r \sin(\theta)/24, \tag{1.4}$$

where

$$Re_r = \rho|\boldsymbol{\omega}|d^2/\mu \tag{1.5}$$

is termed the rotational Reynolds number for characterizing the rotational movement of spheres, and θ is the angle between vectors $\boldsymbol{\omega}$ and $\boldsymbol{U}$. It can be seen in (1.4) that the lift force is in direct proportion to Re_r at small Reynolds numbers.

Later, Saffman (1965) obtained an analytical solution of the lift force acting on a rotating sphere in a linear unbounded shear flow by using matched asymptotic expansions. His expression for the lift force can be given by (Kurose & Komori 1999)

$$F_L = 6.46\nu\rho a^2 U_c(|\alpha_s|/\nu)^{1/2} - 11\rho U_c \alpha_s a^3/8 + \pi\rho U_c \omega a^3, \tag{1.6}$$

where U_c is the fluid velocity on the streamline through the centre of the sphere, a is the radius of the sphere, α_s is the fluid shear rate of the mean flow, and ν is the kinematic viscosity of the fluid. The first two terms on the right-hand side are due to the fluid shear, while the third term represents the Magnus lift force. Saffman commented that unless the rotation speed is significantly greater than the shear rate, and for a freely rotating particle $\omega = \alpha_s/2$, the lift force due to particle rotation is an order of magnitude lower than that due to the shear when the Reynolds number is small. Recently, through direct numerical simulations (DNS), Bagchi & Balachandar (2002) found that, even in finite-Reynolds-number regimes, the lift due to free particle rotation (induced by flow shear) is less significant than shear-induced lift on the particle.

The coupling between the Reynolds number Re and the dimensionless shear rate α_s^* ($\alpha_s^* = \alpha_s a/U_c$) was numerically investigated by Dandy & Dwyer (1990). The results

show that the ratio between the lift force and the drag force is less than 0.07 over all simulated Re ($0.1 \leqslant Re \leqslant 100$) when a relatively large α_s^* is used ($\alpha_s^* = 0.1$). Therefore, only the drag force and particle gravity are considered to be responsible for the dynamics of fluid–particle flows in simulations of many industrially important reactor systems (Zou, Guo & Chan 2008; Xu *et al.* 2012). The Magnus lift force, believed to be even less important than the lift force due to flow shear (the Saffman force), is usually neglected.

Though the free particle rotation only causes very insignificant Magnus lift force, this may not be how the particles behave in realistic gas–solids systems. Many investigators (e.g. Bagnold 1973; White & Schulz 1977) have shown the importance of lifting forces in saltation trajectories of sand grains. Through high-speed motion pictures (2000 f.p.s.), White & Schulz (1977) reported that the saltating spherical glass microbeads were spinning at a rate of several hundred revolutions per second. They pointed out that the high spinning rates are generally obtained by collisions with the sand surface. They also found that including the Magnus lift force can increase the height of sand motion by 50 %, resulting in remarkable agreement between numerical trajectory solutions and the filmed trajectories. These observations and calculations were confirmed by another set of experiments performed by White (1982). Many developments have been made based on White & Schulz's work (e.g. Zou *et al.* 2007; Kang & Zou 2011). It is worth mentioning that Zou *et al.* (2007) reported that in terms of the height and the horizontal distance increases, the Magnus force contributes several times more than the Saffman force does.

With the use of high-speed imaging cameras, investigators found that the majority of particles are rotating at high speeds in circulating fluidized bed (CFB) risers (Wu *et al.* 2008; Shaffer, Shadle & Breault 2009). Experiments show that the high rotating rates are caused by strong frictional collisions, including both inter-particle collisions and particle–wall collisions. Wu *et al.* (2008) reported that the mean and maximum rotating rates of particles with a diameter of 0.5 mm were around 300 rev s^{-1} and 2000 rev s^{-1}, respectively. Considering that the kinematic viscosity of air is around 1.5×10^{-5} m^2 s^{-1}, the rotational Reynolds numbers corresponding to these rotating rates are 30 and 210 respectively. The data from Shaffer *et al.* (2009) yield even larger values of rotational Reynolds number, which are around 90 and 350, respectively. It needs to be mentioned that the rotational Reynolds number due to free particle rotation is usually much less than unity. It is also helpful to use the dimensionless angular speed Γ ($\Gamma = \omega a/U_c$) to characterize the relative importance of the rotational movement (e.g. Tsuji, Morikawa & Mizuno 1985; Kurose & Komori 1999). Here, an equivalent definition of Γ would be $\Gamma = 0.5\,Re_r/Re$ when the angular velocity is perpendicular to the mean flow. In typical CFB risers, while Re_r has a magnitude of $O(10^2)$, as mentioned above Re is usually between $O(10)$ and $O(10^2)$. This makes Γ in the range of $O(1)$ and $O(10)$. For individual particles, Γ may range from zero to $O(10^3)$ since, at some instant, individual particles can be completely non-rotational or rotating fast with an almost vanishing Re. To explore the effects of particle rotation in a wide range of Γ, in this work simulations are performed at a small Re of around 0.2 with Re_r changing from practically zero to $O(10^2)$.

In computational fluid dynamics (CFD), researchers (e.g. Goldschmidt 2001; Sun & Battaglia 2006) have realized that the absence of particle rotation and subsequent energy losses is a deficiency of the multi-fluid model, in contrast to the discrete particle model (DPM), which incorporates physics at the particle level, such as collisions and particle rotation, and simulates particle behaviour that is closer to experimentally observed conditions. After formulating a particle rotation model to

account for the energy dissipation due to particle rotation, Sun & Battaglia (2006) and Wang *et al.* (2012) found that the bubble dynamics and time-averaged bed behaviour were better captured in gas-fluidized beds using the multi-fluid models. The CFD-DPM, also known as CFD-DEM (CFD-discrete element model), was first proposed by Tsuji *et al.* (1987), Tsuji, Tanaka & Ishida (1992), Tsuji, Kawaguchi & Tanaka (1993) and rationalized by Xu & Yu (1997, 1998). This approach gives realistic pictures of particle motion by applying Newton's laws of motion to individual particles. The dynamics of continuum fluid is solved using traditional CFD based on the local averaged Navier–Stokes equations. By this approach, many fluid–particle interaction forces with different physical origins, including the Magnus force, can be implemented in a rather straightforward way (Zhu *et al.* 2007). Using the CFD-DPM with a simple particle–wall collision model, Tsuji *et al.* (1987) investigated the motion of particles and fluid in a horizontal channel. They found that some particles were lifted to a higher position by the Magnus force and thus the particles were dispersed widely in the pipe cross-section. By employing a sticking–sliding collision model to solve the particle–particle collisions and the particle–wall collisions, Lun & Liu (1997) also found that the Magnus force played a significant role in suspending the solid phase in a horizontal channel. They also reported that Re_r of particles ranged from approximately 120 to 1360 for all the simulated cases, which are much greater than the measurements conducted by Wu *et al.* (2008) and Shaffer *et al.* (2009). Schellander, Schneiderbauer & Pirker (2013) developed a new numerical model based on Eulerian–Lagrangian discrete phase approaches and found that the results were significantly improved in terms of the average particle velocity and solid volume fraction. They attributed this improvement to the inclusion of the Magnus force.

To the best of the authors' knowledge, the solution of Rubinow & Keller (1961) is the only available theory for the Magnus force. Unfortunately, their theory is only valid at the zero-solid-volume-fraction limit in the low-Reynolds-number regime. Some researchers (e.g. White & Schulz 1977; Zou *et al.* 2007; Kang & Zou 2011) directly used Rubinow & Keller's solution at all conditions, based on the belief that the Magnus force should be around the same order of magnitude, while other researchers (e.g. Barkla & Auchterlonie 1971; Tsuji *et al.* 1985; Lun & Liu 1997; Oesterle & Dinh 1998; Loth 2008) invested much effort in developing empirical models of the Magnus force based on experimental measurements. Tsuji *et al.* (1985) clearly stated that the Magnus force is proportional to the dimensionless angular speed Γ when Re is in the range from 550 to 1600, indicating that the Magnus force may become very significant when Γ is quite large. Later, Oesterle & Dinh (1998) reported that the proportionality tends to decrease with increasing Γ in the range $10 < Re < 140$. For reviews on empirical models, the reader can refer to Loth (2008) and Crowe *et al.* (2012).

Moreover, DNS of a spinning sphere have been performed to calculate the Magnus force in different Reynolds number regimes (e.g. Kurose & Komori 1999; Zhou & Fan 2014). Kurose & Komori's results showed that, at $Re = 500$, the Magnus force is around 50 % of the drag force when a sphere spins at a large Re_r of 250 (note, in their paper, this spinning rate is represented by Γ with a value of 0.25). The recent simulations by Zhou & Fan (2014) show that, in the low-Reynolds-number flow regime, the Magnus force reaches around 16 % and 65 % of the drag force when a sphere spins at Re_r of 10 and 50, respectively. It should be mentioned that the above investigations, including experimental measurements and numerical simulations, solely pay attention to the Magnus force at the zero limit of solid volume fractions, even though the Reynolds number regime varies. Nevertheless, these investigations,

especially the two DNS studies, have demonstrated that the Magnus force could be significant when particles spin at high speeds. It is therefore very important to conduct more comprehensive computations to evaluate the Magnus force experienced by the rotating particles in particle-laden flows. With regard to the torque acting on rotating spheres, Takagi (1977) and Dennis, Singh & Ingham (1980) have analytically obtained the solution for a rotating sphere in a fluid at rest. However, their theories only gave the result of the torque at practically zero solid volume fraction and the Magnus force was not calculated due to the essentially zero Reynolds number of the flow.

The drag force in the low-Reynolds-number regime has been obtained analytically at various solid volume fractions in both ordered arrays of spheres (Hasimoto 1959; Sangani & Acrivos 1982; Zick & Homsy 1982) and random arrays of spheres (Kim & Russel 1985; Ladd 1990). In these analytical studies, particle rotation is not allowed, and hence, the solutions of the Magnus force and the torque are not pursued.

As mentioned above, the problem of flow through rotating particles is important in many processes involving particle transport and fluidization. In spite of its wide importance, solutions of the Magnus lift force due to particle rotation are generally limited to conditions of practically zero solid volume fractions. The aim of this work is to obtain accurate results that quantify the Magnus force at various solid volume fractions from practically zero to the close-packed limit by using surface-resolved DNS since obtaining the solution using analytical approaches is difficult, if not impossible. The simulations are performed in both ordered arrays and random arrays of spheres. As a starting point, the flow simulated in this work is limited to the low-Reynolds-number regime. Simulations of flows beyond this regime can be done in a similar manner and are left for future work.

2. Numerical methods

The most recently developed immersed boundary–lattice Boltzmann method (IB-LBM) with second-order accuracy is adopted in this work. Several versions of the numerical method with different time schemes are provided in Zhou & Fan (2014). The version with the fourth-order Runge–Kutta scheme is used in this paper.

The mono-disperse arrays of spheres considered in this work have a solid volume fraction

$$c = n(4/3)\pi(a/L)^3, \tag{2.1}$$

where a is the sphere radius, and n is the number of spheres enclosed in a typically cubic computational domain whose volume is L^3. For each simulation case, a is obtained through (2.1) after the specification of c, n and L. In this work, random arrays and the three most common types of ordered arrays are simulated, which are simple cubic (SC), body-centred cubic (BCC) and face-centred cubic (FCC) arrays. For SC, BCC and FCC arrays of spheres, n simply equals 1, 2 and 4, respectively. For random arrays of spheres, n should be large enough to avoid periodic artifacts. In this paper, n is chosen to be 144. It is important to examine the autocorrelation of the fluid velocity to ensure that the computational domain is sufficient to produce accurate results (Tenneti, Garg & Subramaniam 2011). The streamwise (x direction) autocorrelation and the vertical (y direction) autocorrelation of the streamwise velocity are depicted in figures 1(a) and 1(b), respectively. It can be seen that all the autocorrelations decay quickly to near zero values except the streamwise autocorrelation for $c = 0.1$. This indicates that for small solid volume fractions, more particles and larger computational domains may be required for reduced-period artifacts. However, Tenneti *et al.* (2011) have demonstrated that even

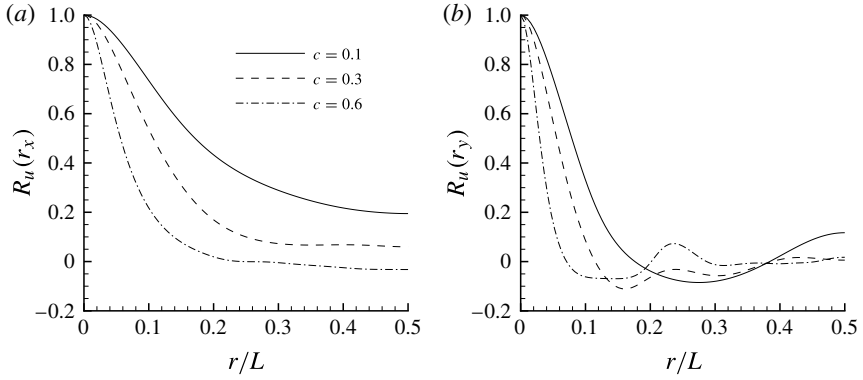

FIGURE 1. The autocorrelation functions of the streamwise velocity obtained from the present simulations of steady Stokes flow past a random configuration of spheres at different solid volume fractions. The grid resolution of the simulations is $L = 192$; r denotes the distance between two points in a specific direction; r_x and r_y denote the autocorrelations calculated in the streamwise and vertical directions, respectively. (a) The streamwise autocorrelation of the streamwise velocity, $R_u(r_x)$; (b) the vertical autocorrelation of the streamwise velocity, $R_u(r_y)$.

simulations with 80 particles could produce satisfactory results for $c = 0.1$. Therefore, in this work, no attempt has been made to simulate more particles for $c = 0.1$. The spanwise (z direction) autocorrelation of the streamwise velocity behaves similarly to the vertical one and thus is omitted here.

In order to reduce statistical uncertainty, several random sphere configurations should be simulated for each solid volume fraction. For each configuration, flows in three different directions are simulated to obtain more independent results for ensemble averaging. In this work, the configuration number for each solid volume fraction is usually two or larger, i.e. at least six independent results are obtained for each solid volume fraction of the random-array simulations. Representing the number of independent results by n_i, the standard deviation of a quantity ϕ is calculated from $\Delta\phi = \sqrt{\langle(\phi - \langle\phi\rangle)^2\rangle/(n_i - 1)}$, where $\langle\phi\rangle$ is obtained through $\langle\phi\rangle = \sum_{j=1}^{n_i} \phi_j/n_i$. In the final average, we intended to omit all values that are outside 2.5 times the standard deviation, as calculated from the initial average. However, no values have been disregarded since all the results are found to be within 2.5 times the standard deviation of the mean. This is attributed to the sophisticated random configuration procedure used in this paper, which is a combination of the standard Monte Carlo procedure (Metropolis *et al.* 1953) and the method of Zinchenko (1994). For details of this procedure, the reader is referred to Hill, Koch & Ladd (2001*a*,*b*).

The simulations are initiated with a flow field at rest. A constant pressure gradient $\nabla p_e = \boldsymbol{b} p_c \rho \nu^2/d^3$ is imposed to drive the flow through fixed assemblies of spheres, where $\boldsymbol{b}$ is a unit vector representing the direction of the pressure gradient and p_c is used to adjust the magnitude of the constant pressure gradient. In this work, p_c is chosen such that Re of the flow is around or smaller than 0.2. It is found that flows with even smaller Re produce indistinguishable forces on spheres, which is consistent with the findings in Van der Hoef, Beetstra & Kuipers (2005).

To obtain the result for each case, a set of simulations with different grid resolutions is executed. Typically, the grid resolutions used here are $L/h = 48$, 72 and 108 for ordered arrays and $L/h = 108$, 144 and 192 for random arrays, where L and h are

the size of the computational cube and the lattice spacing, respectively. The retraction distance of $r_d = 0.3h$ is fixed in all the simulations. The final drag force, Magnus lift force and torque for each case are obtained from Richardson extrapolation using the values from the three consecutive meshes (Breugem 2012; Zhou & Fan 2014). The fluid viscosities adopted in the simulations are computed from $\nu = 1.65\mathrm{CFL}/12$ (Zhou & Fan 2014), where CFL denotes the Courant–Friedrichs–Lewy number. To control the compressibility errors of the LB equation while maintaining the computation stable, CFL is set to 0.8 for solid volume fractions less than 0.3. It is found that compressibility errors grow monotonically with increasing solid volume fraction. Given that compressibility errors can be kept small by either decreasing the fluid viscosity or increasing the ratio of the sphere diameter to the lattice spacing, in this work, CFL is gradually reduced as the solid volume fraction increases to avoid excessively large computational domains. For instance, for random arrays of spheres, the CFL numbers for solid volume fractions $c = 0.4$, 0.5, 0.6 and 0.63 are chosen as 0.4, 0.2, 0.15 and 0.1, respectively. To ensure that the compressible errors are negligible, both the maximum magnitude of the divergence of the velocity field $\boldsymbol{\nabla \cdot u}$ and that of the density fluctuations $\delta\rho$ are recorded during the simulations. It is found that $|\boldsymbol{\nabla \cdot u}|_{max}$ and $|\delta\rho|_{max}$ are usually around 1×10^{-5} and 1×10^{-4} on the finest meshes, respectively, indicating that compressible effects in the simulations can be safely ignored.

2.1. *Calculation of the drag force, the Magnus lift force and the torque acting on spheres*

The overall force $\widetilde{\boldsymbol{F}}$ exerted on a sphere is computed after the flow reaches steady state. In this work, the buoyancy-type force due to the pressure gradient is usually excluded from $\widetilde{\boldsymbol{F}}$. Therefore, $\widetilde{\boldsymbol{F}}$ in stage q of a time step can be calculated as

$$\widetilde{\boldsymbol{F}}^{q} = -\sum_{l} \widetilde{\boldsymbol{F}}_{l}^{q,N_s} \Delta V_l + \frac{\mathrm{d}}{\mathrm{d}t}\left(\int_{V_p} \rho \boldsymbol{u} \mathrm{d}V\right) + V_p \boldsymbol{\nabla} p_e, \tag{2.2}$$

where V_p is the sphere volume, $\boldsymbol{u}$ is the velocity vector of the flow, ΔV_l is the volume for the lth Lagrangian marker, $\widetilde{\boldsymbol{F}}_{l}^{q,N_s}$ is the force experienced by the lth Lagrangian marker, and N_s represents the total number of force iterations in the multi-direct forcing method. The final value of $\widetilde{\boldsymbol{F}}$ is obtained from the following expression:

$$\widetilde{\boldsymbol{F}} = \sum_{k=1}^{i} \beta_{ik} \widetilde{\boldsymbol{F}}^{k}, \tag{2.3}$$

where β_{ik} denotes the coefficients of the Runge–Kutta scheme. Here, $i = 4$ since the four-stage fourth-order Runge–Kutta scheme is used.

It is appropriate to normalize overall force $\widetilde{\boldsymbol{F}}$ with the magnitude of the Stokes drag $\boldsymbol{F}_{DS}$. Thus, we have

$$\boldsymbol{F} = \widetilde{\boldsymbol{F}}/|\boldsymbol{F}_{DS}| = \widetilde{\boldsymbol{F}}/3\pi d\mu\,|\boldsymbol{U}|, \tag{2.4}$$

where $\boldsymbol{F}$ is used to represent the normalized overall force hereinafter. Also, in the remainder of this paper, all the forces referred to are normalized in the same manner and the word 'normalized' is usually omitted for conciseness.

By definition, the drag force $\boldsymbol{F}_D$ is the force experienced by a sphere in the direction of the flow velocity $\boldsymbol{U}$. Denoting the unit vector in the direction of $\boldsymbol{U}$ as

$$\boldsymbol{n}_D = \boldsymbol{U}/\sqrt{\boldsymbol{U}\cdot\boldsymbol{U}}, \tag{2.5}$$

the drag force can be calculated from

$$\boldsymbol{F}_D = F_D\boldsymbol{n}_D = (\boldsymbol{F}\cdot\boldsymbol{n}_D)\boldsymbol{n}_D. \tag{2.6}$$

The lift force due to particle rotation will be in the direction of $-\boldsymbol{\omega}\times\boldsymbol{U}$. Similarly, the unit vector for $-\boldsymbol{\omega}\times\boldsymbol{U}$ is defined as

$$\boldsymbol{n}_L = -\boldsymbol{\omega}\times\boldsymbol{U}/\sqrt{(\boldsymbol{\omega}\times\boldsymbol{U})\cdot(\boldsymbol{\omega}\times\boldsymbol{U})}. \tag{2.7}$$

Then, the lift force can be calculated from

$$\boldsymbol{F}_{L\theta} = F_{L\theta}\boldsymbol{n}_L = (\boldsymbol{F}\cdot\boldsymbol{n}_L)\boldsymbol{n}_L, \tag{2.8}$$

where θ is the angle between $\boldsymbol{\omega}$ and $\boldsymbol{U}$ and can be obtained by

$$\theta = \arcsin[|\boldsymbol{\omega}\times\boldsymbol{U}|/(|\boldsymbol{\omega}|\ \ |\boldsymbol{U}|)]. \tag{2.9}$$

The lift force $\boldsymbol{F}_{L\theta}$ is denoted as $\boldsymbol{F}_L$ only when $\boldsymbol{\omega}$ and $\boldsymbol{U}$ are perpendicular to each other, i.e. $\theta = \pi/2$. The relation between $\boldsymbol{F}_{L\theta}$ and $\boldsymbol{F}_L$ can be expressed as

$$\boldsymbol{F}_{L\theta} = \boldsymbol{F}_L\sin(\theta). \tag{2.10}$$

Theoretically, this relation is valid only when both Re and Re_r are small. However, this work will show that this relation is approximately correct in a wide range of Re_r when Re is small.

In three-dimensional space, the cross-product of two orthogonal unit vectors yields the third unit vector

$$\boldsymbol{n}_R = \boldsymbol{n}_D\times\boldsymbol{n}_L. \tag{2.11}$$

The force along the third unit vector, referred to as the residual force, is calculated from

$$\boldsymbol{F}_R = F_R\boldsymbol{n}_R = (\boldsymbol{F}\cdot\boldsymbol{n}_R)\boldsymbol{n}_R. \tag{2.12}$$

In the low-Reynolds-number regime, the force $\boldsymbol{F}_R$ vanishes in an ordered-array simulation due to the linearity of the Stokes equations and symmetry considerations. However, in a random-array simulation, $\boldsymbol{F}_R$ may be non-zero due to the fact that a perfectly isotropic random configuration is difficult to achieve. Generally, an anisotropic configuration may direct the flow away from the direction of the imposed pressure gradient, making $\boldsymbol{F}$ deviate from $\boldsymbol{U}$ even when particle rotation is not present. This phenomenon has been reported by previous studies (e.g. Kriebitzsch, Van der Hoef & Kuipers 2013; Zhou *et al.* 2014). However, the underlying reason behind it has not been elaborated. Essentially, a phenomenon of this kind is quite common in practice. An extreme but simple example of an anisotropic configuration resembles the shape of an aerofoil, which can be formed by stacking a number of spheres in an organized way. When the fluid flows around an aerofoil, it certainly experiences, other than the drag force, a force in a lateral direction, the so-called aerodynamic

lift force. The difference is that, in the area of aerodynamics, the generation of the lateral force is not solely due to the anisotropic shape of the aerofoil but also to the boundary layer theory at high Reynolds numbers. Here, we will refer to the force caused by the anisotropy of configurations simply as the 'configuration force' and represent it by $\boldsymbol{F}_C$. The direction of the configuration force can be quite arbitrary, depending on the specific positioning of the spheres in arrays. For a system without particle rotation, $\boldsymbol{F}_C$ can be estimated by

$$\boldsymbol{F}_C = \boldsymbol{F} - \boldsymbol{F}_D. \tag{2.13}$$

For a system with particle rotation, the entire $\boldsymbol{F}_R$ and part of $\boldsymbol{F}_L$ come from $\boldsymbol{F}_C$. Certainly, $\boldsymbol{F}_C$ also contributes to $\boldsymbol{F}_D$ in systems with or without particle rotation. This does not affect the accuracy of $\boldsymbol{F}_D$ much since $\boldsymbol{F}_C$ is usually around or less than 1 % of $\boldsymbol{F}_D$ in magnitude. However, $\boldsymbol{F}_C$ can be comparable to or even greater than the actual lift force when the rotational Reynolds number is low. This influence on the lift force cannot be appreciably reduced by averaging over limited samples (for details on this issue, see discussions in § 3.2.2). Therefore, to accurately calculate the lift force, a procedure to eliminate the configuration force must be formulated.

Theoretically, in low-Reynolds-number flows, other than the translational movement, the rotational movement of the particles also contributes to the configuration force in anisotropic random arrays. Thus, essentially, $\boldsymbol{F}_C$ is comprised of $\boldsymbol{F}_C^U$ and $\boldsymbol{F}_C^\omega$, which are the average configuration force caused by the translational and rotational movements of the spheres, respectively. To evaluate the magnitude of $\boldsymbol{F}_C^\omega$, the direct approach is to simulate systems in which spheres rotate but do not translate, i.e. the systems have a non-zero Re_r but a literally zero Re. However, it is not possible to make Re zero without prior knowledge of the force potentially caused by particle rotation. With the linearity of the problem, the configuration force from particle rotation can be easily calculated by conducting simulations with zero pressure gradient. To this end, simulations with $Re_r = 0.1$ are performed at conditions of $\nabla p_e = 0$ for various solid volume fractions. It is found that the fluid in steady state still flows in a certain direction with a very small yet non-zero Reynolds number, which is termed Re' for later use. Since the fluid is flowing with constant velocity, the total force on the fluid should be zero. This yields

$$-L^3 \nabla p_e - n\boldsymbol{F}_{g\to s} = 0, \tag{2.14}$$

where $\boldsymbol{F}_{g\to s}$ is the total average force that the fluid exerts on each sphere (including the buoyancy-type force if the pressure gradient is non-zero). From the analysis above, it follows that

$$\boldsymbol{F}_{g\to s} = \boldsymbol{F}_D + \boldsymbol{F}_L + \boldsymbol{F}_C^U + \boldsymbol{F}_C^\omega - V_p \nabla p_e. \tag{2.15}$$

It is known that $\boldsymbol{F}_C^U$ is independent of particle rotation and is always minor compared to $\boldsymbol{F}_D$. It is also known that for any Re, the magnitude of $\boldsymbol{F}_L$ at $Re_r = 0.1$ is always around 10^{-3} times of that of $\boldsymbol{F}_D$, which is based on the simulation results performed in this work as well as on the theoretical relation (1.4). Keeping these in mind and also considering that $\nabla p_e = 0$, the combination of (2.14) and (2.15) gives

$$\boldsymbol{F}_D + \boldsymbol{F}_C^\omega \approx 0. \tag{2.16}$$

Therefore, the magnitude of $\boldsymbol{F}_C^\omega$ can be estimated by that of $\boldsymbol{F}_D$, which can be easily determined by Re'. Through simulations for various solid volume fractions, it is

learned that the magnitude of Re' is generally around $O(10^{-6})$, which is approximately 10^{-5} times smaller than the Reynolds number used to generate the results in this work, which is around 0.2. This makes the magnitude of $\boldsymbol{F}_C^{\omega}$ approximately 10^{-5} times smaller than that of $\boldsymbol{F}_D$ obtained at $Re \approx 0.2$ due to the linearity of this problem. Also, as just mentioned, the magnitude of $\boldsymbol{F}_L$ is only around 10^{-3} times that of $\boldsymbol{F}_D$ at a small Re_r of 0.1. All this makes $\boldsymbol{F}_L$ calculated at $Re_r = 0.1$ and $Re \approx 0.2$ approximately 10^2 times larger than $\boldsymbol{F}_C^{\omega}$. Moreover, both $\boldsymbol{F}_L$ and $\boldsymbol{F}_C^{\omega}$ are approximately in direct proportion to Re_r, making $\boldsymbol{F}_C^{\omega}$ still negligible compared to $\boldsymbol{F}_L$ for various Re_r up to $O(10^2)$. Therefore, no efforts are made to eliminate $\boldsymbol{F}_C^{\omega}$ in this work. These comparisons also indicate that to obtain accurate results for $\boldsymbol{F}_L$ and $\boldsymbol{F}_D$ for random arrays, Re_r and Re cannot be chosen arbitrarily small, though, analytically, smaller Re_r and Re yield better linearity of the problem. As far as $\boldsymbol{F}_D$ is concerned, Re may be lowered to around $O(10^{-4})$ without significantly affecting the results. However, for better accuracy of $\boldsymbol{F}_L$, Re_r cannot be either too large or too small. A large Re_r will certainly incur the unwanted nonlinearity. Too small a Re_r will yield a small $\boldsymbol{F}_L$ that can be easily contaminated by the configuration force $\boldsymbol{F}_C^{\omega}$. Based on the discussions above, the choice of $Re_r = 0.1$ and $Re \approx 0.2$ is used to produce the results in the present work for flows in the Stokes regime.

Other than the drag force and the Magnus lift force, the torque $\widetilde{\boldsymbol{T}}$ exerted by the fluid on the rotating sphere is also computed in this work. $\widetilde{\boldsymbol{T}}$ in stage q of a time step can be calculated as

$$\widetilde{\boldsymbol{T}}^q = -\sum_l \boldsymbol{r}_l^{q-1} \times \widetilde{\boldsymbol{F}}_l^{q,N_s} \Delta V_l + \frac{\mathrm{d}}{\mathrm{d}t}\left(\int_{V_p} \boldsymbol{r} \times (\rho \boldsymbol{u}) \mathrm{d}V\right), \tag{2.17}$$

where $\boldsymbol{r}$ is the position vector relative to the sphere centroid. Similarly to the overall force $\widetilde{\boldsymbol{F}}$, the final value of $\widetilde{\boldsymbol{T}}$ is obtained from the following expression:

$$\widetilde{\boldsymbol{T}} = \sum_{k=1}^{i} \beta_{ik} \widetilde{\boldsymbol{T}}^k. \tag{2.18}$$

The torque $\widetilde{\boldsymbol{T}}$ due to particle rotation for zero solid volume fraction at low Reynolds numbers has been analytically obtained by Kirchhoff (1876) and Rubinow & Keller (1961) and given by

$$\boldsymbol{T}_{RK} = -\pi \mu d^3 \boldsymbol{\omega}. \tag{2.19}$$

It is appropriate to normalize the torque $\widetilde{\boldsymbol{T}}$ with the magnitude of $\boldsymbol{T}_{RK}$. Hence, the normalized torque $\boldsymbol{T}$ can be calculated as

$$\boldsymbol{T} = T\boldsymbol{n}_T = \widetilde{\boldsymbol{T}} / \pi \mu d^3 |\boldsymbol{\omega}|, \tag{2.20}$$

where T represents the magnitude of the normalized torque $\boldsymbol{T}$ and $\boldsymbol{n}_T$ is the unit direction vector of $\boldsymbol{T}$. In low-Reynolds-number flows, the present simulations show that the direction of the torque $\boldsymbol{T}$ is indistinguishable from the opposite direction of the angular velocity $\boldsymbol{\omega}$ even when the rotational Reynolds number reaches $O(10^2)$. Therefore, $\boldsymbol{n}_T$ can be simply defined by the following expression:

$$\boldsymbol{n}_T = -\boldsymbol{\omega} / \sqrt{\boldsymbol{\omega} \cdot \boldsymbol{\omega}}. \tag{2.21}$$

2.2. *Procedure to eliminate the configuration force*

As mentioned above, the flow is driven by a constant pressure gradient ∇p_e, whose direction can be prescribed at will. Due to the anisotropy of the generated random arrays, the steady-state flow velocity $\boldsymbol{U}$ will not necessarily follow, but instead deviate slightly from, the direction of $-\nabla p_e$. This means that $\boldsymbol{U}$ and hence all the three unit vectors, $\boldsymbol{n}_D$, $\boldsymbol{n}_L$ and $\boldsymbol{n}_R$, cannot be determined until steady state of a simulation is obtained. For a simulation with particle rotation in a random array, the force obtained in the direction of $\boldsymbol{n}_L$ contains both the Magnus lift force and the component of the configuration force in that direction. To calculate and thus eliminate the unwanted configuration force, typically a simulation without particle rotation but with flow in the same direction as the one with particle rotation needs to be performed. Considering that $\boldsymbol{U}$ and the three unit vectors may vary as the flow parameters such as Re_r change, it is very desirable to formulate a procedure that can reproduce the configuration force in arbitrary directions. Thanks to the linearity of Stokes flows, this can be achieved by simulating the flows without particle rotation through the random array in three linearly independent, not necessarily orthogonal, directions. Denoting the three linearly independent directions by $\boldsymbol{n}_{DN1}$, $\boldsymbol{n}_{DN2}$ and $\boldsymbol{n}_{DN3}$, an arbitrary direction $\boldsymbol{n}_D$ in three-dimensional space can be expressed through a linear combination as follows:

$$\boldsymbol{n}_D = \alpha \boldsymbol{n}_{DN1} + \beta \boldsymbol{n}_{DN2} + \gamma \boldsymbol{n}_{DN3}. \tag{2.22}$$

The coefficients α, β and γ are solved using the iterative Gauss–Seidel method due to its simplicity and efficiency. Considering the linearity of Stokes flows, the forces exerted on spheres by the fluid flowing in the direction of $\boldsymbol{n}_D$ can be expressed as

$$\boldsymbol{F}_N = \alpha \boldsymbol{F}_{N1} + \beta \boldsymbol{F}_{N2} + \gamma \boldsymbol{F}_{N3}, \tag{2.23}$$

where $\boldsymbol{F}_{N1}$, $\boldsymbol{F}_{N2}$ and $\boldsymbol{F}_{N3}$ are the overall force exerted on spheres when the flow is in the direction of $\boldsymbol{n}_{DN1}$, $\boldsymbol{n}_{DN2}$ and $\boldsymbol{n}_{DN3}$, respectively. Here, the overall force $\boldsymbol{F}_N$ is the sum of the drag force and the configuration force. The actual Magnus force $\boldsymbol{F}_{L\theta}$ can then be evaluated by eliminating the contribution from the configuration force in the direction of $\boldsymbol{n}_L$, as shown in the expression

$$\boldsymbol{F}_{L\theta} = [(\boldsymbol{F} - \boldsymbol{F}_N) \cdot \boldsymbol{n}_L]\boldsymbol{n}_L. \tag{2.24}$$

Similarly, the influence of particle rotation on residual force can also be evaluated by

$$\boldsymbol{F}_{Rr} = [(\boldsymbol{F} - \boldsymbol{F}_N) \cdot \boldsymbol{n}_R]\boldsymbol{n}_R. \tag{2.25}$$

This force essentially is a projection of $\boldsymbol{F}_C^{\omega}$ on $\boldsymbol{n}_R$ by virtue of the analysis in the previous subsection.

To ensure that the unit vectors $\boldsymbol{n}_{DN1}$, $\boldsymbol{n}_{DN2}$ and $\boldsymbol{n}_{DN3}$ are linearly independent, the pressure gradient used to drive the flow needs to be specified carefully. In this work, the three directions of the pressure gradient for each random array are chosen as follows:

$$\boldsymbol{b}_{N1} = (-1, 0, 0), \quad \boldsymbol{b}_{N2} = (0, -1, 0), \quad \boldsymbol{b}_{N3} = (0, 0, -1). \tag{2.26a–c}$$

Naturally, in isotropic arrays, the flow will follow the direction opposite to that of the pressure gradient, resulting in

$$\boldsymbol{n}_{DN1} = (1, 0, 0), \quad \boldsymbol{n}_{DN2} = (0, 1, 0), \quad \boldsymbol{n}_{DN3} = (0, 0, 1). \tag{2.27a–c}$$

However, due to the existence of anisotropy in the computer-generated random arrays, the actual flow directions may slightly deviate from those shown in (2.27). The actual unit vectors can be written as

$$\boldsymbol{n}_{DN1} = (n_{11}, n_{12}, n_{13}), \quad \boldsymbol{n}_{DN2} = (n_{21}, n_{22}, n_{23}), \quad \boldsymbol{n}_{DN3} = (n_{31}, n_{32}, n_{33}), \qquad (2.28a\text{–}c)$$

in which n_{11}, n_{22}, n_{33} are close to 1 and all other components are near zero, making $\boldsymbol{n}_{DN1}$, $\boldsymbol{n}_{DN2}$ and $\boldsymbol{n}_{DN3}$ linearly independent. This also ensures that the coefficient matrix of (2.22) is diagonally dominant, guaranteeing that the solution of α, β and γ can be obtained.

The procedure to eliminate the configuration force from the Magnus lift force may not be exactly valid when Re_r is in the intermediate range. This is because the linearity property of the flow may have broken down due to the strong disturbance from the fast particle rotation. However, this will not cause a noticeable error in our results since the lift force at relatively large Re_r has significantly surpassed the configuration force in magnitude. Thus, in the present work, the procedure formulated above is applied to all simulations for random arrays. Moreover, it is found that the effects of the configuration force on the torque are negligible.

For ordered arrays of spheres, no configuration force is involved in the simulations due to the symmetric positioning of spheres. The drag force, Magnus lift force and torque can be obtained directly through (2.6), (2.8) and (2.20). The residual force $\boldsymbol{F}_R$ used to indicate the magnitude of the configuration force always stays within the machine round-off errors.

3. Results and analysis

3.1. *Simulations for ordered arrays of spheres*

First, Stokes flows in ordered arrays of spheres are examined without particle rotation. The results for drag forces provide an excellent means of testing the accuracy of the present numerical method over a wide range of solid volume fractions due to the availability of existing theoretical and computational results in the literature. Then, simulations with particle rotation are performed under various conditions.

3.1.1. *The drag force*

The drag force on spheres in SC arrays is shown in figure 2. It can be seen that the results are in excellent agreement with the theory by Zick & Homsy (1982). The differences between the present results and Zick & Homsy's results are relatively larger at high solid volume fractions, where their analytical computations suffer from limited order approximations. Also shown in the figure are the computational results from Hill *et al.* (2001*a*). Their results scatter around the results of Zick & Homsy, which could be caused by the diameter corrections adopted in their simulations. The analytical results by Hasimoto (1959) and Sangani & Acrivos (1982) for dilute cases are also provided in figure 2.

Based on the present simulation results for high solid volume fractions and previous theories for low solid volume fractions, a simple fit for the drag force in the entire packing range is proposed as follows:

$$F_D = \begin{cases} (1-c)(1-1.7601c^{1/3}+c-1.5593c^2+3.9799c^{8/3}-3.0734c^{10/3})^{-1} & (c<0.2), \\ 2.812+2.621c+47.99c^2+16.99c^3 & (0.2\leqslant c\leqslant \pi/6), \end{cases} \qquad (3.1)$$

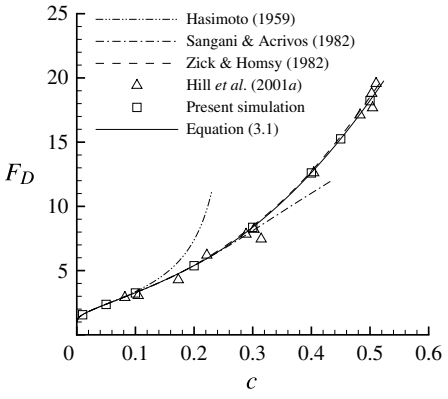

FIGURE 2. The Stokes-flow drag force on non-rotational spheres in SC arrays as a function of the solid volume fraction. The simulation result of Hill *et al.* (2001*a*) and the results from the theories of Hasimoto (1959) and Sangani & Acrivos (1982) are also shown. The dashed line interpolates the discrete results of Zick & Homsy (1982). The solid line represents the fit proposed in this work.

where the equation for $c < 0.2$ is from Sangani & Acrivos's theory and $\pi/6 \approx 0.524$ represents the theoretical packing limit of SC arrays of spheres.

The results for the drag force for BCC and FCC arrays are shown in figure 3, in which it can be seen that the present results agree well with those obtained by Zick & Homsy (1982). The expressions

$$F_D = \begin{cases} (1-c)(1-1.7918c^{1/3}+c-0.3292c^2)^{-1} & (c<0.1), \\ 2.118+6.512c+76.22c^2-163.0c^3+281.5c^4 & (0.1 \leqslant c \leqslant \sqrt{3}\pi/8), \end{cases} \tag{3.2}$$

and

$$F_D = \begin{cases} (1-c)(1-1.7917c^{1/3}+c-0.3020c^2)^{-1} & (c<0.1), \\ \exp(0.6767+5.796c-3.959c^2+4.664c^3) & (0.1 \leqslant c \leqslant \sqrt{2}\pi/6), \end{cases} \tag{3.3}$$

are proposed to fit the present numerical results for BCC and FCC arrays, respectively, in which, $\sqrt{3}\pi/8$ and $\sqrt{2}\pi/6$ represent the theoretical packing limit of BCC and FCC arrays, respectively. The theories of Hasimoto (1959) are used in both expressions for higher accuracy in the low range of solid volume fractions ($c < 0.1$).

3.1.2. *The Magnus lift force and the torque due to particle rotation*

To calculate the Magnus lift force F_L, the spheres in arrays are allowed to rotate at various fixed rates from the low to the intermediate range. For each selected solid volume fraction, usually six values of Re_r are simulated. Specifically, they are 0.1, 1, 10, 50, 100 and 200. The rotation axis of the spheres is first set perpendicular to the direction of the added pressure gradient, as shown in figure 4. The non-perpendicular case is examined afterwards.

Figure 5 shows the drag force, Magnus lift force and torque acting on the sphere in SC arrays as a function of Re_r. It can be seen that in general, in the range of Re_r from practically zero up to $O(10^2)$, the Magnus lift force linearly increases with Re_r,

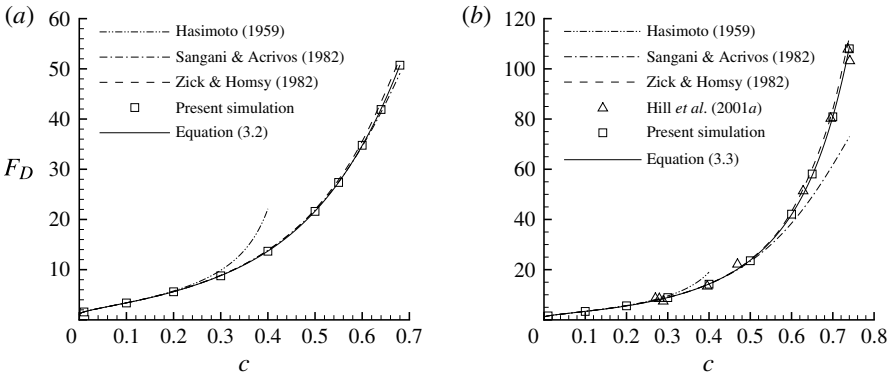

FIGURE 3. As figure 2, but for (*a*) BCC and (*b*) FCC arrays.

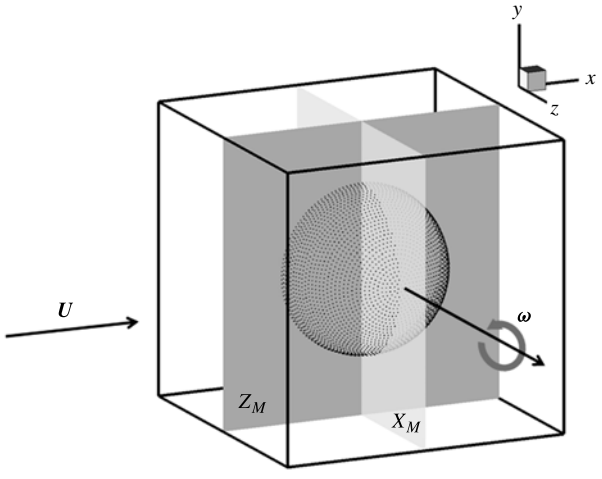

FIGURE 4. Schematic illustration of flow through SC arrays of rotating spheres. A sphere is positioned in the middle of the computational domain and periodic conditions are implemented in three directions. The angular velocity of the sphere $\boldsymbol{\omega}$ is in the positive z direction. The flow velocity $\boldsymbol{U}$ driven by the added pressure gradient is in the positive x direction when particle rotation is absent. Two two-dimensional planes X_M and Z_M through the centre of the sphere, normal to the x and z axes, respectively, are also shown.

whereas the drag force and the torque barely change as Re_r increases. This indicates that in low-Reynolds-number flows, the nonlinearity caused by the intermediate Re_r is insignificant. Based on the present results shown in figure 5, the linear dependence of the lift forces on Re_r can be represented by the following expression:

$$F_L(Re_r) = F_L|_{Re_r=0.1} Re_r/0.1, \tag{3.4}$$

where $F_L|_{Re_r=0.1}$ is the Magnus lift force at $Re_r = 0.1$. The torque can be expressed as

$$T(Re_r) = T|_{Re_r=0.1}, \tag{3.5}$$

and the drag forces can be simply denoted by

$$F_D(Re_r) = F_D|_{Re_r=0}, \tag{3.6}$$

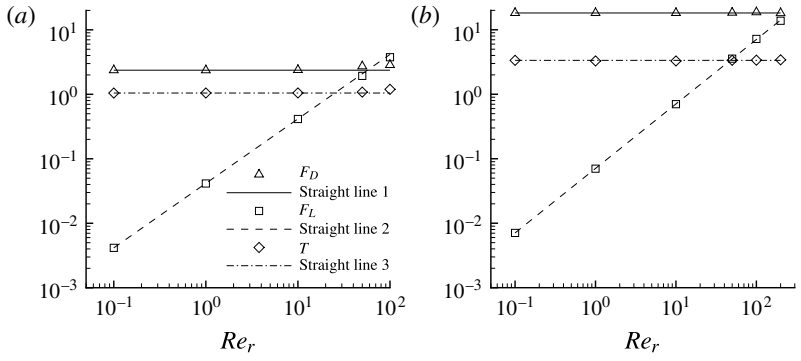

FIGURE 5. The drag force, Magnus lift force and torque as a function of Re_r in low-Reynolds-number flows for SC arrays of spheres. Three straight lines are drawn for reference. 'Straight line 1' is a horizontal line with the constant value of the drag force when particle rotation is absent. 'Straight line 2' is governed by (3.4). 'Straight line 3' is a horizontal line with the constant value of the torque at $Re_r = 0.1$. The solid volume fractions for (*a*) and (*b*) are 0.05 and 0.5, respectively.

where $F_D|_{Re_r=0}$ is the drag force when particle rotation is absent. Close observation reveals that in high Re_r ranges for all solid volume fractions, the Magnus lift forces are slightly lower than the linear prediction made by (3.4) (denoted by 'Straight line 2' in figure 5). This indicates that the nonlinearity due to high Re_r is beginning to set in. For high solid volume fractions, F_L and F_D start to deviate from the linear predictions of (3.4) and (3.6) at relatively larger Re_r. T is the most insensitive quantity to the increase of Re_r. For $c = 0.5$, the deviations at $Re_r = 200$ from (3.5) are only around 2 %. Generally, in the range of $Re_r > 200$, the dependence of F_L, F_D and T on Re_r tends to be more complicated, and is not pursued in the present paper. Overall, the present results show that the lift force can be very significant in view of the magnitude of the drag force when the sphere rotates at high rates. The figure shows that, for the case of $c = 0.05$, F_L is around 32 % larger than F_D at $Re_r = 100$. For $c = 0.5$, F_L is around 39 % and 76 % of F_D at $Re_r = 100$ and $Re_r = 200$, respectively. Considering that the maximum Re_r measured by Wu *et al.* (2008) and Shaffer *et al.* (2009) is around two to three hundred, the values of Re_r simulated here are all within the practical gas–solid flow systems.

To explore specifically why, at high Re_r, the Magnus lift force deviates from the linear relation shown in (3.4), both the contours of steady-state normalized streamwise velocity $u' = u/|\boldsymbol{U}|$ and the streamlines on the middle plane X_M (see figure 4) are shown in figure 6. Figures 6(*a*) and 6(*b*) are the results for $Re_r = 1$ and $Re_r = 100$, respectively. It can be seen that for both Re_r, u' attains negative values at the top and positive values at the bottom of the sphere. This is caused by the particle rotation with $\boldsymbol{\omega}$ directed in the positive z direction (see figure 4). For $Re_r = 1$, the secondary flow on the middle plane transports the fluid from the top to the bottom of the sphere. This flow helps sustain the u' distribution caused by particle rotation, which produces the Magnus lift force. However, for $Re_r = 100$, the secondary flow is dominated by four circulating flows that reside at the corners of the computational cube. This flow pattern hinders the transport of the fluid from the top to the bottom and thus to some degree reduces the difference of u' at the two sides. Eventually, a Magnus lift force lower than expected from the linear relation will be produced. This flow pattern

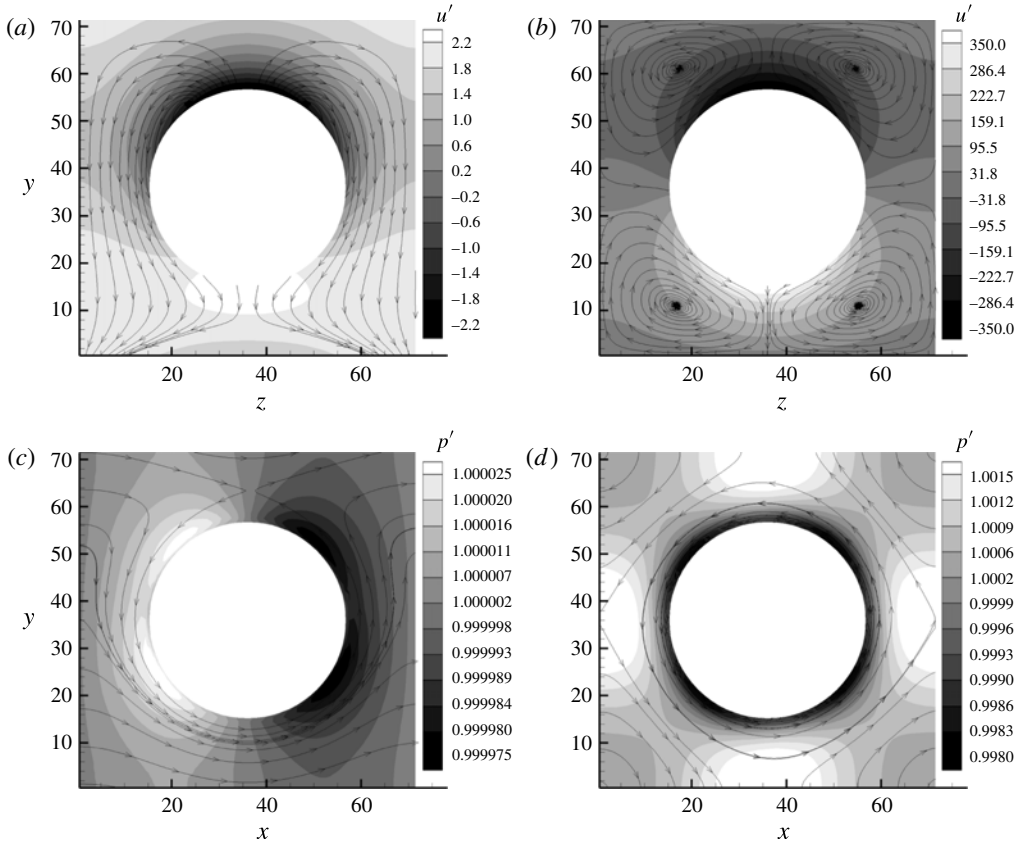

FIGURE 6. (*a,b*) Contours of the steady-state normalized streamwise velocity $u' = u/|\boldsymbol{U}|$ and streamlines on the two-dimensional plane X_M denoted in figure 4. (*c,d*) Contours of the steady-state normalized pressure $p' = p/(\rho_0/3)$ and streamlines on the two-dimensional plane Z_M denoted in figure 4. The results are generated from the simulations for a solid volume fraction of 0.1 at the grid resolution of $L/h = 72$, where L and h are the size of the computational cube and the lattice spacing, respectively. For (*a,c*), $Re_r = 1$ while for (*b,d*), $Re_r = 100$.

also explains why the torque increases slightly at large Re_r (see figure 5) since the inefficient transport of the fluid from the top to the bottom certainly increases the resistance of the rotational motion of the sphere.

Figure 6(*c,d*) shows the distribution of the normalized pressure p' on the two-dimensional plane Z_M, where the position of plane Z_M is denoted in figure 4. In LBM, the pressure is computed as $\rho/3$ and hence the normalized pressure is defined as $p' = p/(\rho_0/3)$, where ρ_0 is the initial density of the fluid in the simulation. It can be seen that for $Re_r = 1$, high and low pressure appears upstream and downstream of the sphere separately, while for $Re_r = 100$, the pressure distribution becomes approximately symmetric around the sphere. The symmetric pressure distribution is essentially caused by the fast rotation motion of the sphere, which promotes an instant communication of the flow information between upstream and downstream (see the streamlines in figure 6(*d*)). This pressure distribution tends to decrease the overall force experienced by the sphere and thus the Magnus lift force would be lower than

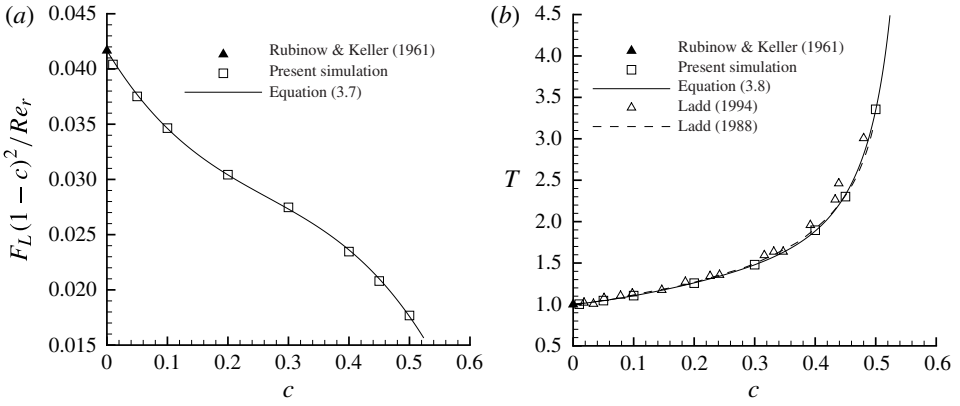

FIGURE 7. (*a*) The Magnus lift force F_L multiplied by the porosity squared divided by the rotational Reynolds number on the rotational spheres in SC arrays as a function of the solid volume fraction. (*b*) The torque T on the rotational spheres in SC arrays as a function of the solid volume fraction: the dashed line is the numerical solution of the Stokes equations (Ladd 1988); the open triangles represent the results obtained using a LBM by Ladd (1994). Also shown in (*a,b*) are solid lines representing the best fit to the present results at $Re_r = 0.1$ and the theoretical results calculated by Rubinow & Keller (1961) at zero solid volume fraction.

the prediction from the linear relation. Moreover, it is noted that the decreasing trend of F_L with increasing Re_r has been observed in experiments at intermediate Reynolds numbers performed by Oesterle & Dinh (1998). However, definitive explanations of this trend were not given because no information on the flow structure can be obtained from their experiments.

Due to the linear dependence of the lift forces on Re_r, the expression for F_L for various solid volume fractions can be developed solely based on the results obtained at small Re_r. Figure 7(*a*) depicts F_L multiplied by $(1-c)^2$ divided by Re_r as a function of c. The values are from the computations at $Re_r = 0.1$, which is small enough to provide accurate proportionalities for higher Re_r. In order to best fit the present simulation results and also have the correct limiting behaviour for $c \to 0$, a third-order polynomial is proposed for F_L as follows:

$$F_L(1-c)^2/Re_r = (-0.287c^3 + 0.228c^2 - 0.0904c + 1/24). \tag{3.7}$$

The largest deviation of this fit from the present numerical results is less than 1 %.

For the torque, an expression is proposed as follows:

$$T = (-14.09c^4 + 10.26c^3 - 2.916c^2 - 0.7480c + 1)^{-1}. \tag{3.8}$$

This fit naturally produces the correct results at the limit of vanishing c, which is $T = 1$ predicted by Rubinow & Keller (1961) as well as Kirchhoff (1876). The largest deviation of this fit from the present numerical results is less than 1 %. The results for the torque over a wide range of solid volume fractions are also confirmed by the numerical solution of the Stokes equations (Ladd 1988) and the simulation results by Ladd (1994), which are shown in figure 7(*b*).

The effect of the angle between the rotation axis of the sphere and the flow direction is also explored in this work. Figure 8 depicts ratios of the Magnus lift

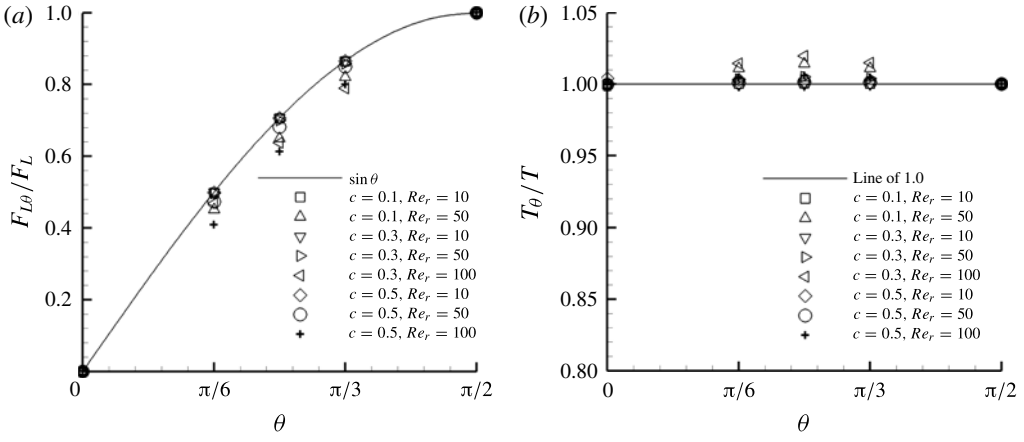

FIGURE 8. (*a*) The ratios of the Magnus lift force at several selected angles $\theta = 0$, $\pi/6$, $\pi/4$ and $\pi/3$ to the Magnus lift force at $\theta = \pi/2$; (*b*) the same as (*a*), but for the torque.

force and the torque at several selected angles of $\theta = 0$, $\pi/6$, $\pi/4$ and $\pi/3$, to their values at $\theta = \pi/2$, respectively. Generally, the torque and the drag force (not shown) stay basically unchanged as θ varies. The lift force is found to be approximately proportional to $Re_r \sin(\theta)$, which is the rotational Reynolds number defined by the component of the angular velocity perpendicular to the flow direction. Thus, for arbitrary rotation axis directions and solid volume fractions, the dependence of the Magnus force on the rotational Reynolds number can be well described by

$$F_L(Re_r; \theta; c) = Re_r \sin(\theta)(-0.287c^3 + 0.228c^2 - 0.0904c + 1/24)/(1-c)^2 \quad (c \leqslant \pi/6). \tag{3.9}$$

The drag force relation, (3.1), and the torque relation, (3.8), still apply regardless of the values of Re_r and θ due to their insensitivity to these rotation-related parameters. It should be mentioned that at high rotational Reynolds numbers, the nonlinearity of the flow starts to set in and produces deviations from (3.8) and (3.9), as one can observe from figures 5 and 8. In the range of smaller rotational Reynolds number, $Re_r < 10$, (3.1), (3.8) and (3.9) can be used for all the solid volume fractions with less than 1 % error. For larger Re_r, the errors of these relations generally decrease as the solid volume fraction increases. For low solid volume fractions, $c < 0.1$, (3.1), (3.8) and (3.9) can be used in the range of $Re_r < 50$ with errors less than approximately 5 %, 2 % and 15 %, respectively. While for high solid volume fractions, $c > 0.3$, with almost the same error thresholds, these relations can be used up to approximately $Re_r = 100$.

The results for the Magnus lift force and the torque for BCC and FCC arrays are depicted in figure 9. The proposed expressions for the Magnus lift force for BCC and FCC arrays are

$$F_L(1-c)^2/Re_r = (-0.0478c^3 + 0.0853c^2 - 0.0890c + 1/24) \quad (c \leqslant \sqrt{3}\pi/8) \tag{3.10}$$

and

$$F_L(1-c)^2/Re_r = (-0.0546c^3 + 0.0992c^2 - 0.0930c + 1/24) \quad (c \leqslant \sqrt{2}\pi/6), \tag{3.11}$$

respectively. The expressions for the torque for BCC and FCC arrays are

$$T = (-2.890c^4 + 2.924c^3 - 1.154c^2 - 0.8444c + 1)^{-1} \quad (c \leqslant \sqrt{3}\pi/8) \tag{3.12}$$

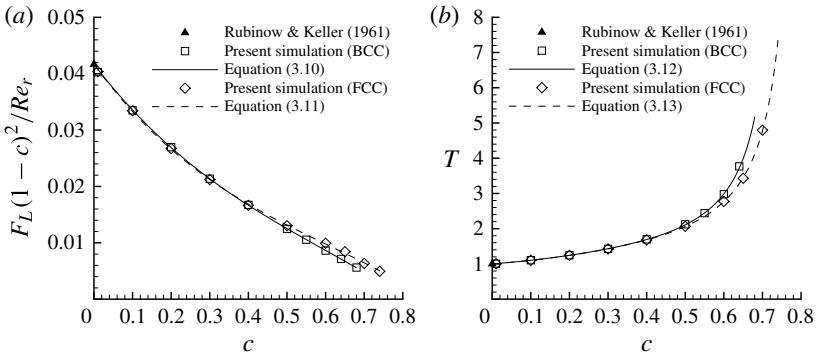

FIGURE 9. (*a*) The Magnus lift force F_L multiplied by the porosity squared over the rotational Reynolds number on the rotational spheres in BCC and FCC arrays as a function of the solid volume fraction. (*b*) The torque T on the rotational spheres in BCC and FCC arrays as a function of the solid volume fraction. Also shown in (*a,b*) are the theoretical results calculated by Rubinow & Keller (1961) at zero solid volume fraction.

and

$$T = (-2.280c^4 + 2.568c^3 - 1.093c^2 - 0.8406c + 1)^{-1} \quad (c \leqslant \sqrt{2}\pi/6), \tag{3.13}$$

respectively. Similar to SC arrays, more general Magnus lift relations for BCC and FCC arrays accounting for arbitrary rotation axis directions can be obtained.

3.2. *Simulations for random arrays of spheres*

3.2.1. *The drag force*

Following the procedure outlined in § 2, simulations without particle rotation are performed to calculate the drag force F_D for random arrays of spheres. Figure 10 compares the present results with previous numerical results (Ladd 1990; Hill *et al.* 2001*a*,*b*; Van der Hoef *et al.* 2005), theoretical predictions (Carman 1937; Kim & Russel 1985; Koch & Sangani 1999) and an empirical fit based on experimental results (Wen & Yu 1966). The figure shows that the present results agree well with previous numerical values and the Carman relation. The standard errors in F_D of the present results are typically less than 5 % of the mean (not shown). Based on the present simulation results, the best fit for the drag force in random arrays is proposed as follows:

$$F_D = \begin{cases} 9.9c/(1-c)^2 + (1-c)^3(1+3c^{0.6}) & (c < 0.55), \\ 5.87\sin\left((c/0.637)^{1.75}\pi/2\right)/(1-c)^2 & (0.55 \leqslant c \leqslant 0.637), \end{cases} \tag{3.14}$$

where 0.637 is the packing limit of a randomly packed bed of mono-disperse spheres in experiments (Scott & Kilgour 1969). In the range of $c < 0.55$, the present expression takes a similar form to Van der Hoef *et al.*'s equation. The maximum difference between this expression and the present results is less than 3 %.

3.2.2. *The Magnus lift force and the torque due to particle rotation*

For random-array systems, the evaluation of the Magnus lift force can be very complex since, in practical situations, particles may rotate at different speed rates

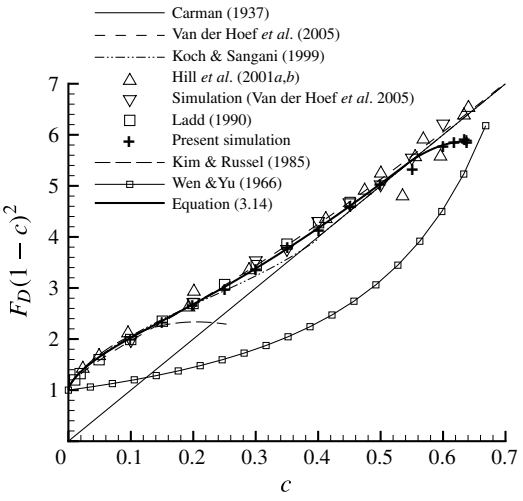

FIGURE 10. The Stokes-flow drag force F_D (multiplied by the porosity squared) on the non-rotational spheres in random arrays as a function of the solid volume fraction. The simulation results of Ladd (1990), Hill *et al.* (2001*a*,*b*) and Van der Hoef *et al.* (2005) are represented by symbols. The results from the theories of Carman (1937), Kim & Russel (1985), Koch & Sangani (1999) and Van der Hoef *et al.* (2005) and the empirical fit of Wen & Yu (1966) are also shown.

with different rotation axis directions. In this section, a first step is made towards describing the Magnus lift force for practical systems, where all spheres are forced to rotate with the same angular velocity $\boldsymbol{\omega}$. Thus, the reported mean Magnus lift force can also be interpreted as an average force experienced by one sphere in various local microstructures due to particle rotation. In the simulations, the rotation axis of the sphere is set to be perpendicular to the direction of the added pressure gradient. However, it may not be perpendicular to the computed superficial flow velocity $\boldsymbol{U}$ due to the existence of the configuration force. Since the configuration force is minor relative to the drag force, the angle θ between $\boldsymbol{\omega}$ and the steady-state $\boldsymbol{U}$ is close to but not necessarily equal to $\pi/2$. In this work, it is found that in low-Reynolds-number flows, the relation $F_{L\theta} = F_L \sin(\theta)$ (see (2.10)) holds for a wide range of Re_r not only for ordered arrays but also for random arrays of spheres. Thus, the Magnus lift force at $\theta = \pi/2$ can be recovered by $F_L = F_{L\theta}/\sin(\theta)$.

The simulation results of F_L are given in table 1. The standard deviations in F_L are also shown in this table, which can be up to approximately 10 % of the mean, especially in the low solid volume fraction range. Also shown in table 1 are the results of the torque T and its standard deviation ΔT. Typically, ΔT is only around 1 % of T, indicating that T is not as sensitive to different random configurations. The Magnus lift force calculated without the procedure of eliminating the configuration force, F'_L, and its relative standard deviation $\Delta F'_L/|F'_L|$, are also presented in table 1. It can be seen that F'_L fluctuates in a wide range and $\Delta F'_L/|F'_L|$ attains relatively large values, which indicates that F'_L is not well converged with the limited samples simulated in this work. As pointed out by Tenneti & Subramaniam (2014), even without eliminating the configuration force, ensemble averaging over an adequate number of configurations will yield accurate results. This idea certainly applies to F_L as well as F_D and T. However, based on the results of F'_L shown in table 1, it can be concluded that to obtain accurate results for F_L with direct ensemble averaging, many

c	F_L	$\Delta F_L/F_L$	F'_L	$\Delta F'_L/\lvert F'_L\rvert$	T	$\Delta T/T$
0.1000	0.00350	0.06	−0.00727	5.1	1.22	0.007
0.1500	0.00362	0.10	−0.01250	5.0	1.34	0.010
0.2000	0.00373	0.12	−0.05550	1.3	1.48	0.008
0.2500	0.00385	0.07	0.02940	3.6	1.64	0.020
0.3000	0.00383	0.11	−0.06520	0.76	1.82	0.030
0.3500	0.00419	0.04	−0.14800	1.5	2.00	0.009
0.4000	0.00430	0.07	−0.06090	4.5	2.20	0.006
0.4500	0.00423	0.06	−0.00139	150	2.42	0.010
0.5000	0.00465	0.05	−0.35900	1.2	2.78	0.010
0.5500	0.00487	0.06	−0.63800	1.0	3.38	0.030
0.6000	0.00516	0.07	−0.13800	5.2	4.37	0.050
0.6150	0.00495	0.05	0.05640	7.9	5.22	0.007
0.6300	0.00512	0.12	−0.60900	1.6	6.78	0.006
0.6340	0.00495	0.02	1.02000	1.1	7.06	0.010
0.6345	0.00480	0.03	2.21000	0.59	7.11	0.001

TABLE 1. The Magnus lift force F_L and torque T in random arrays of rotational spheres with $Re_r = 0.1$ at various solid volume fractions c. F'_L is the Magnus lift force calculated without eliminating the configuration force. ΔF_L, $\Delta F'_L$ and ΔT are the standard deviations in F_L, F'_L and T, respectively.

more simulations over different configurations should be performed, which would consume vast computer resources and is not practical.

Similar to ordered arrays, the Magnus lift force increases linearly with increasing Re_r while the drag force and the torque barely change as Re_r varies. Figure 11(*a*) depicts the combination $F_L(1-c)^2/Re_r$ as a function of the solid volume fraction c. The values of F_L come from the simulations at $Re_r = 0.1$. Also shown in this figure are the error bars that represent the standard deviations in F_L. The magnitudes of the error bars are calculated from the results shown in table 1. This figure shows that the dependence of $F_L(1-c)^2/Re_r$ on c is approximately linear. The best fit to describe this dependence is proposed as follows:

$$F_L(1-c)^2/Re_r = -0.0398c + 0.0317 \quad (c \leqslant 0.637). \tag{3.15}$$

The maximum difference in the entire range of packing fractions between this relation and the simulation results is only around 5 %, providing good support for the observed linear dependence. It is noted that the Magnus lift force in random arrays is smaller than that in ordered arrays at all solid volume fractions. This is because the random positioning allows some spheres to stay closer to each other and makes spheres hidden behind others experience a smaller flow velocity and consequently, produce less Magnus lift force.

As $F_{L\theta} = F_L \sin(\theta)$ yields the Magnus lift force for the case where the angle between the angular velocity $\boldsymbol{\omega}$ and the steady-state $\boldsymbol{U}$ is θ, a more general Magnus lift relation for arbitrary rotation axis directions and solid volume fractions in random arrays of spheres can be given as

$$F_L(Re_r; \theta; c) = Re_r \sin(\theta)(-0.0398c + 0.0317)/(1-c)^2 \quad (c \leqslant 0.637). \tag{3.16}$$

The torque on rotational spheres in random arrays as a function of the solid volume fraction is depicted in figure 11(*b*). These results also come from the simulations at

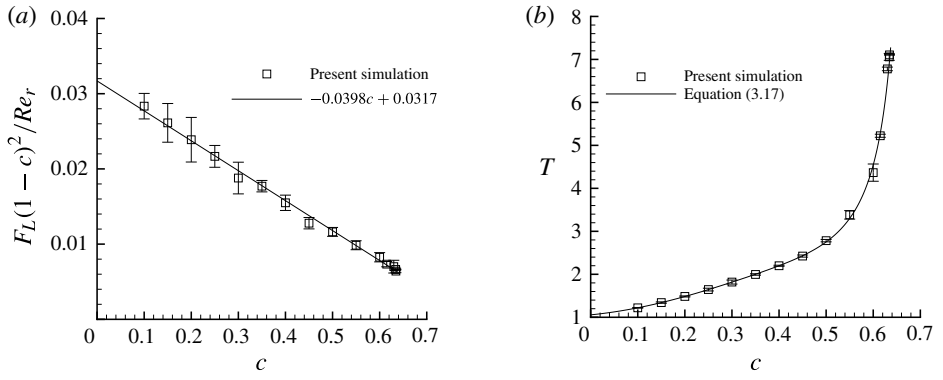

FIGURE 11. (*a*) The Magnus lift force F_L (multiplied by the porosity squared divided by the rotational Reynolds number) on the rotational spheres in random arrays as a function of the solid volume fraction. (*b*) The torque T on the rotational spheres in random arrays as a function of the solid volume fraction. The error bars in (*a*) and (*b*) represent the standard deviations in F_L and T, respectively. The results of F_L and T come from the simulations at $Re_r = 0.1$.

$Re_r = 0.1$. It has been illustrated above that T remains nearly constant with increasing Re_r up to $O(10^2)$ and only a slight deviation is observed at large Re_r. Therefore, the results at a small Re_r, such as $Re_r = 0.1$, are sufficient to represent the value of T for up to $O(10^2)$ for each solid volume fraction. To best fit the results for all the packing fractions, the following expression is proposed:

$$T = (-13.19c^4 + 14.41c^3 - 4.291c^2 - 0.9747c + 0.9465)^{-1} \quad (c \leqslant 0.637). \tag{3.17}$$

The largest deviation of this fit from the present numerical results is less than 1 % for $c \leqslant 0.5$ and around 5 % for $c > 0.5$. The larger deviation at high c is apparently related to the sharp increase of T in that range (see figure 11(*b*)), which essentially is caused by the dramatically shrinking space among spheres as c approaches the packing limit. Similar to ordered arrays, the drag relation, (3.14), and the torque relation, (3.17), hold in a wide range of Re_r regardless of the value of θ.

3.2.3. *Simulations for random arrays of spheres with random angular velocities*

In real gas–solid systems, freely moving particles may rotate at different rates with different rotation axis directions. To move a step closer to real-world systems, even in the systems with fixed particles, it is helpful to examine how random angular velocities will affect the results for the systems. In this section, it is assumed that the angular velocities of real systems follow a Gaussian distribution. The assignment of random angular velocities to particles is done as follows. First, all the particles are given the same prescribed mean angular velocity $\boldsymbol{\omega}$ as done in § 3.2.2. Then, the angular velocity disturbances, which essentially are Gaussian random values with zero mean and a specific standard deviation σ, are added to the components in three directions of the angular velocity of all particles. Applying the central limit theorem (Rice 1995), the angular velocity disturbances can be generated by repeatedly running Fortran's random number generator routines. To produce more physically sound results, the standard deviation σ of the disturbances is allowed to increase as the magnitude of the mean $\boldsymbol{\omega}$ increases. Thus, for different $\boldsymbol{\omega}$, σ is

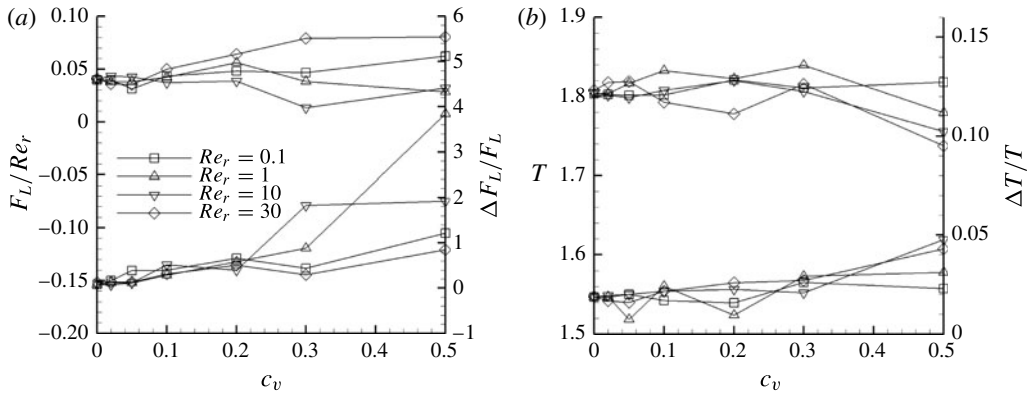

FIGURE 12. (*a*) The Magnus lift force F_L/Re_r on the rotational spheres in random arrays (upper lines) and its relative standard deviation $\Delta F_L/F_L$ (lower lines) as a function of the coefficient of variation c_v. (*b*) The same as (*a*), but for the torque T and its relative standard deviation $\Delta T/T$. The simulations are performed at a solid volume fraction of 0.3.

calculated by $\sigma = c_v|\boldsymbol{\omega}|$, where c_v is termed the coefficient of variation. It also needs to be kept in mind that $|\boldsymbol{\omega}|$ is always determined by (1.5) once Re_r is prescribed.

Figure 12 depicts the results for F_L/Re_r and T and their relative standard deviations $\Delta F_L/F_L$ and $\Delta T/T$ as a function of c_v. For each discrete c_v, four cases with $Re_r = 0.1$, 1, 10 and 30 are simulated. It can be seen that as c_v increases, the values of F_L/Re_r and T begin to fluctuate around those obtained in the cases of vanishing c_v, where angular velocity disturbances for particles are absent. This fluctuation of the mean values become more evident when c_v is larger than 0.1. Due to the relatively stronger nonlinearity associated with larger Re_r, the magnitude of the fluctuation increases with the increase of Re_r. For instance, at $c_v = 0.1$, the maximum deviations of F_L/Re_r and T relative to the results at $c_v = 0$ occur at $Re_r = 30$, which are around 25 % and 1.6 %, respectively. Figure 12 also shows that the relative standard deviations $\Delta F_L/F_L$ and $\Delta T/T$ increase as c_v increases. It is also noted that the influence of the randomness in the angular velocities on F_D is not strong and similar to that on T. The fluctuation of the mean values and the increase of the relative standard deviations of the results appear to be due to the limited samples (generally six samples) used to generate these results. These phenomena are intrinsically caused by two reasons. One is that the randomness in angular velocities makes the flow possess more microstructures and hence such a system cannot be fully represented with a relatively small number of particles. The other reason is associated with the nonlinearity of the flow brought in by relatively fast-rotating particles, which disturb the local flow strongly and the effects on particles still persist after the average is performed. Moreover, the number of fast-rotating particles increases with increasing c_v. This adds further complexity to the problem and makes the relative standard deviations even larger.

Simulations in this section are only performed for a solid volume fraction of 0.3. Nevertheless, the results do demonstrate that systems primarily considered in this paper in which particles are all rotating in unison are good approximations of real systems with weak randomness of angular velocities ($c_v < 0.1$).

3.3. *The ratio of the Magnus lift force to the drag force*

To clearly identify the importance of the Magnus lift force F_L relative to the drag force F_D in both SC arrays and random arrays of spheres, the ratio of F_L to F_D is calculated

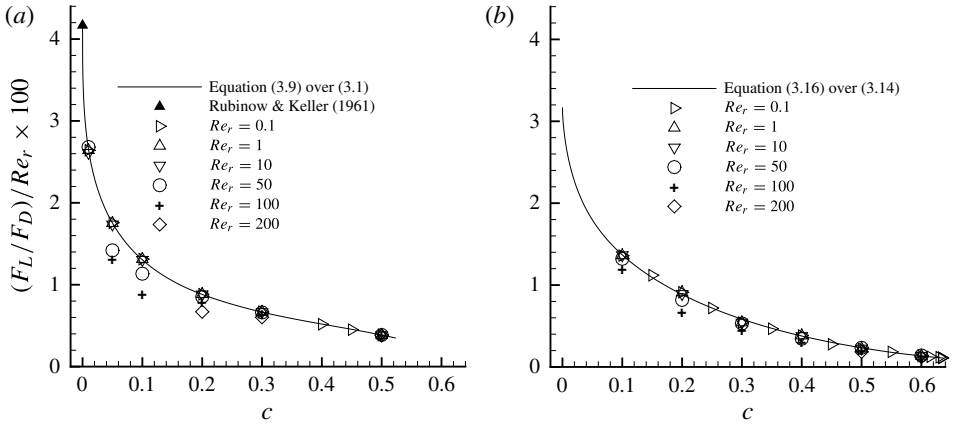

FIGURE 13. The ratio of the Magnus lift force F_L to the drag force F_D on the rotational spheres as a function of the solid volume fraction: (*a*) the results for SC arrays of spheres; (*b*) the results for random arrays of spheres.

in the entire range of solid volume fractions c based on the simulation results as well as the relations proposed in previous subsections. For simplicity, only the values of F_L at $\theta = \pi/2$ are used. The results for SC arrays and random arrays of spheres are shown in figures 13(*a*) and 13(*b*), respectively. The line in figure 13(*a*) is calculated by dividing the lift relation, (3.9), by the drag relation, (3.1), while the line in figure 13(*b*) is calculated by dividing the lift relation, (3.16), by the drag relation, (3.14). For both arrays of spheres, it can be seen that the ratio of F_L to F_D first decreases rapidly in the range of $c < 0.1$ then slows down as c further increases. Most of the simulation results agree well with the line calculated from the proposed relations except those at $Re_r > 50$ for low solid volume fractions, which is due, as mentioned above, to the appearance of the nonlinearity of the flow.

Figure 13 shows that the lift force can be very significant and even greater than the drag force when Re_r is up to $O(10^2)$, which is still in the practical range as mentioned in the Introduction. Close observation reveals that for both arrays of spheres, when Re_r reaches 100, the lift-to-drag ratio will be more than unity in the range of c of less than approximately 0.17. In the range of high solid volume fractions, $c > 0.3$, the lift force can be safely ignored only when Re_r is less than 10, where the lift-to-drag ratio is generally less than 0.07. However, the lift force can still be significant when spheres are rotating at high rates. For instance, when $Re_r = 100$, the lift-drag-ratio for $c = 0.3$ and 0.5 is around 67 % and 39 %, respectively, for SC arrays of spheres, and around 58 % and 23 %, respectively, for random arrays of spheres. The Magnus lift force, appearing in a direction perpendicular to the drag force with a non-negligible magnitude, may appreciably change and complicate the particle fluid dynamics in practical flow systems. Thus, the inclusion of the Magnus lift force is of practical importance in flow simulations. Fortunately, it has been shown that the Magnus lift force can be readily included in the CFD–DPM (Zhu *et al.* 2007). The inclusion of the Magnus lift force in multi-fluid models is somewhat non-trivial due to the fact that rotating speeds of spheres are not tracked in these models. Still, some potential approaches to solving this problem have been proposed in the literature (see Lun 1991; Jenkins & Zhang 2002; Sun & Battaglia 2006).

4. Summary

In the present study, steady low-Reynolds-number flows in both ordered arrays and random arrays of non-rotational and rotational spheres are examined over the entire range of packing fractions. The drag forces of the non-rotational spheres in both arrays show good agreement with corresponding existing theories and numerical results. For SC, BCC and FCC arrays of spheres, relations for the drag force equations (3.1)–(3.3), are proposed based on the analytical solutions by Hasimoto (1959) and Sangani & Acrivos (1982) at low solid volume fractions and the present simulation results at intermediate and high solid volume fractions. These are the first drag force relations that cover the entire solid volume fractions for the three ordered arrays. For random arrays of spheres, based on the present simulation results, a revised relation for the drag force (3.14) is proposed with minor corrections to the one formulated by Van der Hoef *et al.* (2005).

To compute the Magnus lift force due to particle rotation, a procedure is formulated to eliminate the influence of the configuration force produced by the anisotropic random arrays of spheres. This procedure applies only for low-Reynolds-number flows where the linearity of the Stokes equations prevails. It is found that the Magnus lift force produced by the rotation movement is approximately in direct proportion to the rotational Reynolds number in the range from practically zero up to $O(10^2)$, while the drag force and the torque are barely affected by the rotational Reynolds number. Through the evaluation of the ratio between the Magnus lift force and the drag force, it is demonstrated that other than the drag force, the Magnus lift force can be another important factor affecting the overall particle–fluid dynamics. Based on the present simulation results, the Magnus lift force relations, (3.9), (3.10), (3.11) and (3.16), as well as the torque relations, (3.8), (3.12), (3.13) and (3.17), are proposed for the ordered SC, BCC, FCC arrays and random arrays of spheres, respectively. These are the first relations proposed that cover all possible packing fractions. In addition, the effect of the angle between the rotation axis of the sphere and the flow direction is also explored. It is found that the lift force is proportional to the rotational Reynolds number defined by the component of the angular velocity perpendicular to the flow direction. The drag force and the torque are basically unaffected by varying the angle of the rotation axis.

To move a step closer to real-world freely evolving suspensions of mono-disperse spherical particles, the influence of random angular velocities on the results is examined. For random angular velocities with small relative standard deviations (coefficient of variation less than 0.1), the results obtained in systems in which particles are all rotating in unison still persist. For random angular velocities with larger relative standard deviations, the drag force, the Magnus lift force and the torque start to fluctuate and their standard deviations generally increase with the increase of the strength of the randomness in angular velocities. The major reasons for this are discussed in § 3.2.3.

Finally, it should be pointed out that the Magnus lift force has usually been ignored in previous studies of fluid–solid systems. That could be mainly due to unawareness of the fast rotation speeds of particles occurring in practical systems and the lack of Magnus lift force relations for practical random arrays of particles. Recognizing the fast rotation speeds of particles inherently present in the process systems, as experimentally confirmed in the literature and with the relations obtained in this study, the impact of the Magnus lift force on the particle–fluid dynamics in flows can be assessed with ease since the obtained relations can be readily implemented in the CFD–DPM, which is a popular Eulerian–Lagrangian method used for particle–fluid

simulations. It should be noted that the present Magnus lift relations can only be used in low-Reynolds-number flows. Calculations of the Magnus lift force in intermediate- and high-Reynolds-number flows are in progress.

Acknowledgements

This work was supported in part by an allocation of computing time from the Ohio Supercomputer Center. The financial support by the US Department of Energy grant no. FE0007520 is gratefully acknowledged. Helpful discussion with Dr K. C. Kwon is appreciated. We would also like to thank Dr A. Z. Zinchenko for his sharing of the code that generates close-packed random sphere configurations used in this work.

REFERENCES

ANDERSON, J. D. 2005 Ludwig Prandtl's boundary layer. *Phys. Today* **58** (12), 42–48.

BAGCHI, P. & BALACHANDAR, S. 2002 Effect of free rotation on the motion of a solid sphere in linear shear flow at moderate *Re*. *Phys. Fluids* **14**, 2719–2737.

BAGNOLD, R. A. 1973 The nature of saltation and of 'bedload' transport in water. *Proc. R. Soc. Lond.* A **332**, 473–504.

BARKLA, H. M. & AUCHTERLONIE, L. J. 1971 The Magnus or Robins effect on rotating spheres. *J. Fluid Mech.* **47**, 437–447.

BREUGEM, W. P. 2012 A second-order accurate immersed boundary method for fully resolved simulations of particle-laden flows. *J. Comput. Phys.* **231**, 4469–4498.

CARMAN, P. C. 1937 Fluid flow through a granular bed. *Trans. Inst. Chem. Engrs Lond.* **15**, 150–156.

CROWE, C., SCHWARZKOPF, J. D., SOMMERFELD, M. & TSUJI, Y. 2012 *Multiphase Flows with Droplets and Particles*, 2nd edn. CRC Press.

DANDY, D. & DWYER, H. A. 1990 A sphere in linear shear flow at finite Reynolds number: effect of shear on particle lift, drag, and heat transfer. *J. Fluid Mech.* **216**, 381–410.

DENNIS, S. C. R., SINGH, S. N. & INGHAM, D. B. 1980 The steady flow due to a rotating sphere at low and moderate Reynolds numbers. *J. Fluid Mech.* **101**, 257–279.

GOLDSCHMIDT, M. 2001 Hydrodynamic modelling of fluidised bed spray granulation. PhD thesis, Twente University, Netherlands.

HASIMOTO, H. 1959 On the periodic fundamental solution of the Stokes equations and their application to viscous flow past a cubic array of spheres. *J. Fluid Mech.* **5**, 317–328.

HILL, R. J., KOCH, D. L. & LADD, A. J. C. 2001*a* The first effects of fluid inertia on flows in ordered and random arrays of spheres. *J. Fluid Mech.* **448**, 213–241.

HILL, R. J., KOCH, D. L. & LADD, A. J. C. 2001*b* Moderate-Reynolds-number flows in ordered and random arrays of spheres. *J. Fluid Mech.* **448**, 243–278.

JENKINS, J. T. & ZHANG, C. 2002 Kinetic theory for identical, frictional, nearly elastic spheres. *Phys. Fluids* **14** (3), 1228–1235.

KANG, L. & ZOU, X. Y. 2011 Vertical distribution of wind-sand interaction forces in aeolian sand transport. *Geomorphology* **125**, 361–373.

KIM, S. & RUSSEL, W. B. 1985 Modelling of porous media by renormalization of the Stokes equation. *J. Fluid Mech.* **154**, 269–286.

KIRCHHOFF, G. 1876 *Vorlesungen uber Mathematische Physik: Mechanik*. Teubner.

KOCH, D. L. & SANGANI, A. S. 1999 Particle pressure and marginal stability limits for homogeneous monodisperse gas fluidized bed: kinetic theory and numerical simulations. *J. Fluid Mech.* **400**, 229–263.

KRIEBITZSCH, S. H. L., VAN DER HOEF, M. A. & KUIPERS, J. A. M. 2013 Drag force in discrete particle models – continuum scale or single particle scale? *AIChE J.* **59** (1), 316–324.

KUROSE, R. & KOMORI, S. 1999 Drag and lift forces on a rotating sphere in a linear shear flow. *J. Fluid Mech.* **384**, 183–206.

LADD, A. J. C. 1988 Hydrodynamic interactions in a suspension of spherical particles. *J. Chem. Phys.* **88**, 5051–5063.

LADD, A. J. C. 1990 Hydrodynamic transport coefficients of random dispersions of hard spheres. *J. Chem. Phys.* **93**, 3484–3494.

LADD, A. J. C. 1994 Numerical simulations of particulate suspensions via a discretized Boltzmann equation. Part 2. Numerical results. *J. Fluid Mech.* **271**, 311–339.

LOTH, E. 2008 Lift of a solid spherical particle subject to vorticity and/or spin. *AIAA J.* **46** (4), 801–809.

LUN, C. K. K. 1991 Kinetic theory for granular flow of dense, slightly inelastic, slightly rough, spheres. *J. Fluid Mech.* **233**, 539–559.

LUN, C. K. K. & LIU, H. S. 1997 Numerical simulation of dilute turbulent gas–solid flows in horizontal channels. *Intl J. Multiphase Flow* **23**, 575–605.

METROPOLIS, N., ROSENBLUTH, A. W., ROSENBLUTH, M. N., TELLER, A. H. & TELLER, E. 1953 Equation of state calculations by fast computing machines. *J. Chem. Phys.* **21**, 1087–1092.

OESTERLE, B. & DINH, T. B. 1998 Experiments on the lift of a spinning sphere in a range of intermediate Reynolds numbers. *Exp. Fluids* **25**, 16–22.

RICE, J. A. 1995 *Mathematical Statistics and Data Analysis*, 2nd edn. Duxbury Press.

RUBINOW, S. I. & KELLER, J. B. 1961 The transverse force on a spinning sphere moving in a viscous fluid. *J. Fluid Mech.* **11** (3), 447–459.

SAFFMAN, P. G. 1965 The lift on a small sphere in a slow shear flow. *J. Fluid Mech.* **22**, 385–400.

SANGANI, A. S. & ACRIVOS, A. 1982 Slow flow through a periodic array of spheres. *Intl J. Multiphase Flow* **8**, 343–360.

SCHELLANDER, D., SCHNEIDERBAUER, S. & PIRKER, S. 2013 Numerical study of dilute and dense poly-dispersed gas–solid two-phase flows using an Eulerian and Lagrangian hybrid model. *Chem. Engng Sci.* **95**, 107–118.

SCOTT, G. D. & KILGOUR, D. M. 1969 The density of random close packing of spheres. *Brit. J. Appl. Phys.* **2** (2), 863–866.

SHAFFER, F., SHADLE, L. & BREAULT, R. 2009 High speed particle imaging: visualization and measurement of high concentration particle flow. In *US Department of Energy National Energy Technology Laboratory (NETL) Multiphase Flow Workshop, Morgantown, WV, April 22–23*.

SUN, J. & BATTAGLIA, F. 2006 Hydrodynamic modeling of particle rotation for segregation in bubbling gas-fluidized beds. *Chem. Engng Sci.* **61**, 1470–1479.

TAKAGI, H. 1977 Viscous flow induced by slow rotation of a sphere. *J. Phys. Soc. Japan* **42**, 319–325.

TENNETI, S., GARG, R. & SUBRAMANIAM, S. 2011 Drag law for monodisperse gas–solid systems using particle-resolved direct numerical simulation of flow past fixed assemblies of spheres. *Intl J. Multiphase Flow* **37**, 1072–1092.

TENNETI, S. & SUBRAMANIAM, S. 2014 Particle-resolved direct numerical simulation for gas–solid flow model development. *Annu. Rev. Fluid Mech.* **46**, 199–230.

TSUJI, Y., KAWAGUCHI, T. & TANAKA, T. 1993 Discrete particle simulation of 2-dimensional fluidized-bed. *Powder Technol.* **77**, 79–87.

TSUJI, Y., MORIKAWA, Y. & MIZUNO, O. 1985 Experimental measurement of the Magnus force on a rotating sphere at low Reynolds numbers. *Trans. ASME: J. Fluids Engng* **107**, 484–488.

TSUJI, Y., MORIKAWA, Y., TANAKA, T., NAKATSUKASA, N. & NAKATANI, M. 1987 Numerical simulation of gas–solid two-phase flow in a two-dimensional horizontal channel. *Intl J. Multiphase Flow* **13** (5), 671–684.

TSUJI, Y., TANAKA, T. & ISHIDA, T. 1992 Lagrangian numerical simulation of plug flow of cohesionless particles in a horizontal pipe. *Powder Technol.* **71**, 239–250.

VAN DER HOEF, M. A., BEETSTRA, R. & KUIPERS, J. A. M. 2005 Lattice-Boltzmann simulations of low-Reynolds-number flow past mono- and bidisperse arrays of spheres: results for the permeability and drag force. *J. Fluid Mech.* **528**, 233–254.

WANG, S., HAO, Z., LU, H., YANG, Y., XU, P. & LIU, G. 2012 Hydrodynamic modeling of particle rotation in bubbling gas-fluidized beds. *Intl J. Multiphase Flow* **39**, 159–178.

WEN, C. Y. & YU, Y. H. 1966 Mechanics of fluidization. *Chem. Engng Symp. Ser.* **62**, 100–111.

WHITE, B. R. 1982 Two-phase measurements of saltating turbulent boundary layer flow. *Intl J. Multiphase Flow* **8**, 459–473.

WHITE, B. R. & SCHULZ, J. C. 1977 Magnus effect in saltation. *J. Fluid Mech.* **81**, 497–512.

WU, X., WANG, Q., LUO, Z., FANG, M. & CEN, K. 2008 Experimental study of particle rotation characteristics with high-speed digital imaging system. *Powder Technol.* **181**, 21–30.

XU, B. H. & YU, A. B. 1997 Numerical simulation of the gas–solid flow in a fluidized bed by combining discrete particle method with computational fluid dynamics. *Chem. Engng Sci.* **52**, 2785–2809.

XU, B. H. & YU, A. B. 1998 Comments on the paper 'Numerical simulation of the gas–solid flow in a fluidized bed by combining discrete particle method with computational fluid dynamics' – reply. *Chem. Engng Sci.* **53**, 2646–2647.

XU, M., CHEN, F., LIU, X., GE, W. & LI, J. 2012 Discrete particle simulation of gas–solid two-phase flows with multi-scale CPU-GPU hybrid computation. *Chem. Engng J.* **207–208**, 746–757.

ZHOU, G., XIONG, Q., WANG, L., WANG, X., REN, X & GE, W. 2014 Structure-dependent drag in gas–solid flows studied with direct numerical simulation. *Chem. Engng Sci.* **116**, 9–22.

ZHOU, Q. & FAN, L. S. 2014 A second-order accurate immersed boundary-lattice Boltzmann method for particle-laden flows. *J. Comput. Phys.* **268**, 269–301.

ZHU, H. P., ZHOU, Z. Y., YANG, R. Y. & YU, A. B. 2007 Discrete particle simulation of particulate systems: theoretical developments. *Chem. Engng Sci.* **62**, 3378–3392.

ZICK, A. A. & HOMSY, G. M. 1982 Stokes flow through periodic arrays of spheres. *J. Fluid Mech.* **115**, 13–26.

ZINCHENKO, A. Z. 1994 Algorithm for random close packing of spheres with periodic boundary conditions. *J. Comput. Phys.* **114**, 298–306.

ZOU, L. M., GUO, Y. C. & CHAN, C. K. 2008 Cluster-based drag coefficient model for simulating gas–solid flow in a fast-fluidized bed. *Chem. Engng Sci.* **63**, 1052–1061.

ZOU, X. Y., CHENG, H., ZHANG, C. L. & ZHAO, Y. Z. 2007 Effects of the Magnus and Saffman forces on the saltation trajectories of sand grain. *Geomorphology* **90**, 11–22.